https://doi.org/10.5194/egusphere-2025-6248
Preprint. Discussion started: 31 March 2026

Optimizing WRF physics for multi-decadal simulation of near-surface climate over arid Xinjiang, China

Yang Xu[1,2,3], Liang Zhang[4], Mengxin Bai[5], Shenzhen Tian[3], Zhixin Hao[1,2*]
(1. Key Laboratory of Land Surface Pattern and Simulation, Institute of Geographic Sciences and Natural Resources Research, Chinese Academy of Sciences, Beijing, China
2. University of Chinese Academy of Sciences, Beijing, China
3. School of Geographical Sciences, Liaoning Normal University, Dalian, China
4. Department of Natural Resources and the Environment, University of Connecticut, Storrs, United States
5. Beijing Municipal Climate Center, Beijing Meteorological Service, Beijing, China)
Corresponding author: Zhixin Hao, email: haozx@igsnrr.ac.cn

Abstract: Complex terrain, heterogeneous surfaces, and diverse moisture sources complicate mesoscale modeling in arid and semi-arid regions. To evaluate the performance of Weather Research and Forecasting (WRF) model physics in Xinjiang, we tested 34 combinations of physical parameterizations to simulate near-surface climate variables for 1960–2020 and evaluated the simulations against surface observations. Overall skill was highest for 2 m air temperature and surface pressure, moderate for 10 m wind speed and 2 m relative humidity, and lowest for precipitation. Surface downward shortwave radiation was systematically overestimated in spring and summer. Sensitivity analyses show that the Betts–Miller–Janjic (BMJ) cumulus and WRF double-moment 6-class (WDM6) microphysics schemes improve precipitation simulation, while the Mellor–Yamada–Nakanishi–Niino (MYNN) planetary boundary layer scheme improves the representation of wind speed and relative humidity. Configurations using the Simplified Arakawa–Schubert (SAS) or Tiedtke cumulus schemes perform better for surface downward shortwave radiation, and the Community Land Model version 4 (CLM4) improves simulations of temperature and surface pressure. A multi-variable composite evaluation identifies an ensemble-optimal physics suite consisting of Thompson microphysics, Tiedtke cumulus, Rapid Radiative Transfer Model (RRTM) longwave and Dudhia shortwave radiation schemes, the Grenier–Bretherton–McCaa (GBM) planetary boundary layer scheme, the Revised MM5 surface-layer scheme, and the Noah-MP land surface model. This configuration provides the most balanced performance across variables and offers a reference for regional climate simulation in arid and semi-arid regions.

https://doi.org/10.5194/egusphere-2025-6248
Preprint. Discussion started: 31 March 2026

1. Introduction

Arid and semi-arid regions are among the most sensitive and vulnerable to climate change, where the climate system exhibit strong responses to external forcing with far-reaching consequences for ecological sustainability and socio-economic development (Yao et al., 2022). Located in the core of the mid-latitude continental arid belt of Central Asia, Xinjiang exhibits complex mountain–basin physiography and an arid climate with pronounced spatial and seasonal variability in temperature and precipitation (Xu et al., 2024). This geographic–climatic setting amplifies process complexity and poses substantial challenges for numerical weather and climate modeling (Hobbs et al., 2020).

Among available regional models, the Weather Research and Forecasting (WRF) model is a central tool for studying weather and climate over arid, complex terrain because of its flexible physical parameterizations and multiscale capability. Recent applications across China demonstrate strong fidelity in simulating heavy precipitation, wind fields, and climate variability. For precipitation, WRF has reproduced the spatiotemporal variability of the snow-to-precipitation ratio (Li et al., 2018), and advances in data assimilation have substantially improved precipitation analyses in arid regions (Yang et al., 2018; Liu et al., 2021; Liu et al., 2022). During extreme events, WRF has clarified key moisture-transport pathways and the dynamical mechanisms underlying heavy rainfall, including the combined influence of Central Asian vortices, jet streams, and orographic lifting (Jin et al., 2023; Zhao et al., 2021; Shen et al., 2024). For wind and wind-energy studies, incorporating high-resolution land-use data and satellite products has improved simulations of wind speed and wind-energy density, supporting wind-power development (Li et al., 2023). In climate-change applications, WRF is commonly used as a regional climate model for dynamical downscaling, translating large-scale forcing into physically consistent, high-resolution projections of temperature, humidity, evapotranspiration, and orographic precipitation over complex terrain; such downscaled simulations indicate significant precipitation increases over the Tianshan region and suggest the combined roles of global warming and regional human activities (Du et al., 2021; Zhang et al., 2023b). Collectively, these studies underscore WRF's strengths for representing regional processes and climate variability in arid, topographically complex environments.

WRF offers a broad suite of physical parameterizations spanning land-surface processes, planetary boundary-layer (PBL) dynamics, microphysics, and cumulus convection. The choice of individual schemes—and, critically, their combinations—can strongly influence simulation accuracy and process sensitivity. A central challenge is that different schemes can preferentially improve different processes. For example, in the East Asian monsoon environment—where precipitation spans organized stratiform rain to short-lived deep convection—scheme choice can shift both the partitioning and intensity of rainfall: the KF cumulus scheme is often competitive for general stratiform–convective precipitation, whereas Grell-type schemes may exhibit advantages specifically under heavy-rainfall regimes (Yang et al.,

https://doi.org/10.5194/egusphere-2025-6248
Preprint. Discussion started: 31 March 2026

2021; Gao et al., 2022). Another widely recognized difficulty arises in tropical cyclones, where rainfall and wind depend on coupled microphysics–radiation–cumulus interactions; multi-suite evaluations show that selecting a coherent combination (e.g., WSM6 microphysics with RRTMG radiation and KF cumulus) can substantially improve typhoon rainfall, and appropriate physics choices likewise enhance wind and wave simulations (Tian et al., 2021; Luo et al., 2023).

These examples highlight that optimal physics choices are process- and scale-dependent. This dependence is particularly strong in arid, topographically complex Xinjiang, where uncertainty is amplified by (i) convection-parameterization sensitivity under terrain-modulated, intermittent rainfall, (ii) microphysics control on orographic precipitation efficiency and phase, and (iii) biases in stable boundary-layer mixing and land-surface fluxes across deserts, oases, and high mountains. Despite existing evaluations, identifying a robust physics suite for long-term simulations remains challenging, and simulated hydroclimate responses still vary substantially across plausible configurations (Lu et al., 2021; Wang et al., 2021; Zhang et al., 2023c; Li et al., 2022; Yang et al., 2025).

In Xinjiang and adjacent Central Asian arid regions, WRF performance is highly physics-dependent, and an appropriate physics suite can measurably reduce errors in the processes that are hardest to simulate over an arid mountain–basin system. For Tianshan heavy precipitation, studies show that coherent physics choices can improve the timing, intensity, and spatial placement of terrain-modulated rainfall, indicating a practical route to better event-scale realism (Koecher et al., 2023; Chen et al., 2023; Liu et al., 2020). Land–atmosphere exchange presents a parallel challenge: across deserts, oases, irrigated cropland, and snow-influenced mountains, improved land-surface formulations enhance surface fluxes and soil moisture, which helps constrain near-surface temperature–humidity biases that otherwise propagate into evapotranspiration and hydroclimatic diagnostics (Lu et al., 2021; Li et al., 2022; Benson and Dirmeyer, 2023). Regional evaluations further suggest that updated physics formulations can improve the climatological distributions of precipitation and temperature across Xinjiang, reinforcing that scheme choice shapes both extremes and the mean hydroclimate relevant to climate-change studies (Zhang et al., 2023b).

Despite this progress, important gaps remain in physics evaluation for Xinjiang and similar arid regions. (1) Most studies emphasize short-term or case-based simulations, limiting inference about stability and adaptability on multi-decadal climate scales. (2) The scope of variables is often narrow, frequently centered on precipitation, with fewer comprehensive, multi-variable assessments including temperature, wind speed, humidity, radiation, and surface pressure. (3) Cross-season comparisons remain limited, a critical shortcoming in Xinjiang where monsoon–westerly interactions and mountain–basin contrasts yield highly complex seasonal regimes. (4) Systematic evaluations of multiple physics suites constrained by long-term observations are scarce, hindering robust conclusions about long-term applicability for climate-change studies in arid regions. To address these gaps, we design 34 physics-scheme combinations and conduct long-term WRF simulations for 1960–2020 over Xinjiang. We evaluate multiple variables (precipitation, temperature, wind speed, relative humidity, surface downward shortwave radiation, and surface pressure) across seasons against observational datasets to quantify the long-term adaptability and stability of individual schemes and scheme combinations under Xinjiang’s complex topography and arid climate. We aim to identify optimal physics configuration, thereby providing methodological guidance and, ultimately, a practical reference for conducting high-accuracy climate simulations and research on climate-change in arid regions.

2. Data and Methods

2.1 Study Area

Xinjiang, in northwestern China at the core of the Eurasian continent, is a typical mid-latitude inland arid region with complex topography. The Tianshan Mountains run west–east, separating climatically distinct northern and southern subregions. Northern Xinjiang is influenced by the mid-latitude westerlies and intermittent moisture transport from the Arctic Ocean, yielding a comparatively humid climate and higher vegetation cover. Southern Xinjiang lies under the influence of subtropical high pressure and strong orographic shielding, resulting in sparse precipitation, hot and dry conditions, and extensive desert surfaces. The regional landform is commonly summarized as "three mountain ranges enclosing two basins": the Altai, Tianshan, and Kunlun Mountains interspersed with the Junggar and Tarim basins. Elevation gradients are large, and relief is pronounced. Multi-year mean air temperature follows a "warmer south–cooler north" pattern, with extremely hot summers in the basins and perennial cold in high terrain. Over the past six decades, the region has warmed significantly, at a rate exceeding the global average. Precipitation shows a "more in the north, less in the south" distribution, exceeding 500 mm yr⁻¹ in the mountains but falling below 50 mm yr⁻¹ in the basins, with a modest upward trend in recent decades. This combination of unique geographic settings, complex terrain, and sharp climatic contrasts makes Xinjiang a natural laboratory for climate-change studies and numerical modeling in arid regions.

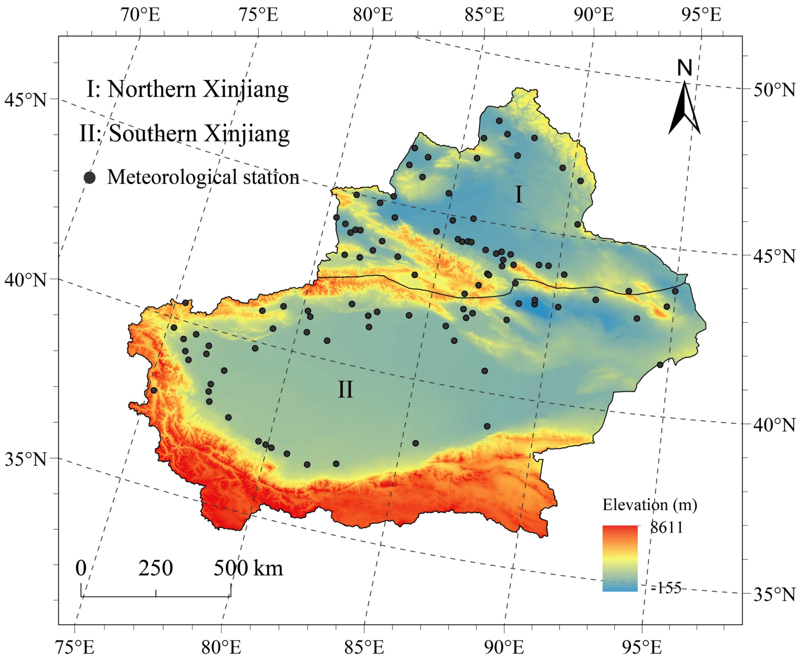

Figure 1. Geographic overview of Xinjiang and distribution of meteorological observation stations.

https://doi.org/10.5194/egusphere-2025-6248
Preprint. Discussion started: 31 March 2026

2.2 Data Sources

2.2.1 Meteorological Observations

Daily station data were obtained from the China National Ground Meteorological Station Daily Dataset (version 3.0) of the National Meteorological Information Center, China Meteorological Administration (CMA; https://data.cma.cn/). The dataset includes 105 national-level stations across Xinjiang (Fig. 1) for 1961–2020, providing maximum, minimum, and mean temperature, precipitation, mean surface pressure, mean wind speed, relative humidity, and sunshine duration. Temperature, pressure, wind, and humidity were observed at 02:00, 08:00, 14:00, and 20:00 local time. Precipitation totals were recorded for the 20:00–08:00 and 08:00–20:00 periods. All data underwent quality control and homogeneity checks, ensuring suitability for model evaluation.

2.2.2 ERA5 Reanalysis

ERA5, produced by the European Centre for Medium-Range Weather Forecasts (ECMWF), is the latest global atmospheric reanalysis (Hersbach et al., 2020). It is available hourly on a 0.25° × 0.25° grid from 1950 to the present and is generated with a four-dimensional variational (4D-Var) data assimilation system coupled to an updated numerical weather prediction model. Relative to ERA-Interim, ERA5 provides higher spatial–temporal resolution, broader variable coverage, and improved accuracy through assimilation of extensive observational data. In this study, ERA5 provided initial and lateral boundary conditions for the WRF simulations. Surface variables included skin temperature, precipitation, surface pressure, mean sea-level pressure, and soil temperature and moisture. Upper-air fields were taken on 37 pressure levels from 1000 to 1 hPa and included wind components, temperature, geopotential height, relative humidity, divergence, vorticity, and vertical velocity.

2.2.3 Topography

Topography was taken from the Advanced Spaceborne Thermal Emission and Reflection Radiometer Global Digital Elevation Model (ASTER GDEM v003; NASA/JAXA), with 30 m horizontal resolution and near-global land coverage. Compared with earlier versions, v003 improves absolute accuracy, spatial continuity, and artifact correction. Original GeoTIFF tiles were mosaicked and converted to ENVI format to generate WRF terrain inputs, enabling a more realistic representation of complex relief.

2.2.4 Land Use/Land Cover

Land-cover data were taken from the Moderate Resolution Imaging Spectroradiometer (MODIS) MCD12Q1 v061 global product (NASA/USGS), at 500 m resolution with 23 land-cover classes (e.g. forest, grassland, cropland, wetland, urban, water). For WRF preprocessing, the data were reprojected from the native sinusoidal grid to a geographic coordinate system and reformatted as land-use inputs.

2.3 Methods

2.3.1 Evaluation Metrics

To quantitatively assess the performance of the WRF simulations, we employed three standard statistical metrics: mean error (ME), Pearson correlation coefficient (CC), and root-mean-square error (RMSE). Let x_i and y_i denote the observed and simulated values, respectively and let $\bar{x}$ and $\bar{y}$ be their means. With n samples, the metrics are defined as

$$ME = \frac{1}{n}\sum_{i=1}^{n}(y_i - x_i) \tag{1}$$

$$CC = \frac{\sum_{i=1}^{n}(x_i-\bar{x})(y_i-\bar{y})}{\sqrt{\sum_{i=1}^{n}(x_i-\bar{x})^2}\sqrt{\sum_{i=1}^{n}(y_i-\bar{y})^2}} \tag{2}$$

$$RMSE = \sqrt{\frac{1}{n}\sum_{i=1}^{n}(x_i - y_i)^2} \tag{3}$$

In addition, we adopted the composite Distance between Indices of Simulation and Observation (DISO) metric, which synthesizes CC, normalized RMSE (NRMSE), and normalized ME (NME) in a three-dimensional coordinate space. NRMSE and NME are defined as

$$NRMSE = \frac{RMSE}{|\bar{y}|} \tag{4}$$

$$NME = \frac{ME}{|\bar{y}|} \tag{5}$$

DISO is then given by

$$DISO = \sqrt{(CC-1)^2 + (NRMSE)^2 + (NME)^2} \tag{6}$$

Smaller DISO values indicate better overall agreement between simulations and observations.

2.3.2 Experimental Design

(1) WRF Configuration

We used WRF for dynamical downscaling with two-way nested domains. The outer domain (D01) had 30 km grid spacing (149 × 145 grid points), and the inner domain (D02) had 10 km grid spacing (202 × 172 grid points), centered at 40° N, 85° E and covering Xinjiang and adjacent regions (Fig. 2). The model employed 40 vertical levels, a 90 s time step, and hourly output. To limit numerical drift and error accumulation in long integrations, we adopted a segmented-run strategy. Each segment spanned 5 days; the first day served as spin-up, and the model was re-initialized at the start of each segment using ERA5. This approach improves stability and reduces drift in long-period climate simulations.

https://doi.org/10.5194/egusphere-2025-6248
Preprint. Discussion started: 31 March 2026

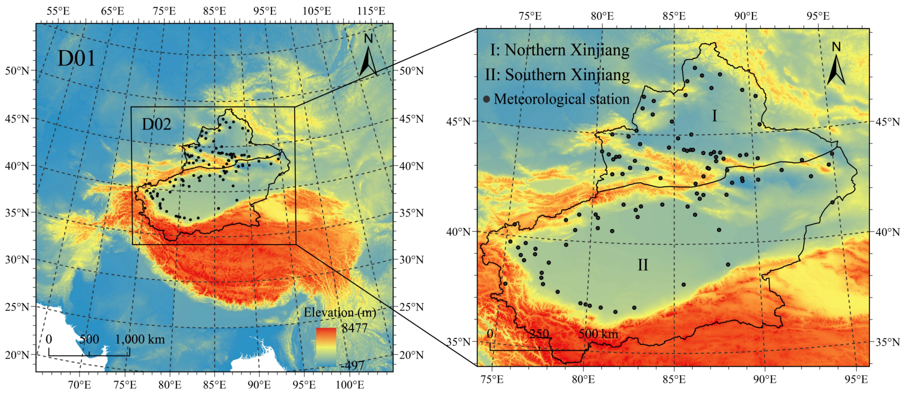

Figure 2. WRF nested domains (D01: 30 km; D02: 10 km) and station locations within D02.

(2) Physics-suite design

WRF provides multiple physics options suitable for different resolutions, terrains, and climate regimes. Based on prior applications in Xinjiang, we selected eight microphysics schemes, eight cumulus schemes, five longwave radiation schemes, seven shortwave radiation schemes, seven planetary boundary-layer schemes, one surface-layer scheme, and four land-surface models (Table 1). A full factorial combination of these options would be required on the order of 60 000 simulations and is computationally infeasible. We therefore adopted a controlled-perturbation strategy: starting from a commonly used “baseline” configuration for Xinjiang, we modified one physics category at a time, yielding 34 physics-suite combinations for sensitivity testing (Table 2). Simulations were performed for seven representative years (1960, 1970, 1980, 1990, 2000, 2010, and 2020). For each year, we selected four representative months (January, April, July, and October) and simulated days 2–27 (26 days) in each month to sample seasonal variability. In total, 28 month-long segments were simulated. Model results were evaluated against concurrent station observations to assess the applicability of each physics combination and to identify an optimal configuration for climate simulation over arid, complex terrain. We systematically evaluated 34 WRF physics suites and selected the single configuration that best represents the observed near-surface meteorology over arid Xinjiang, following the workflow shown in Fig. 3.

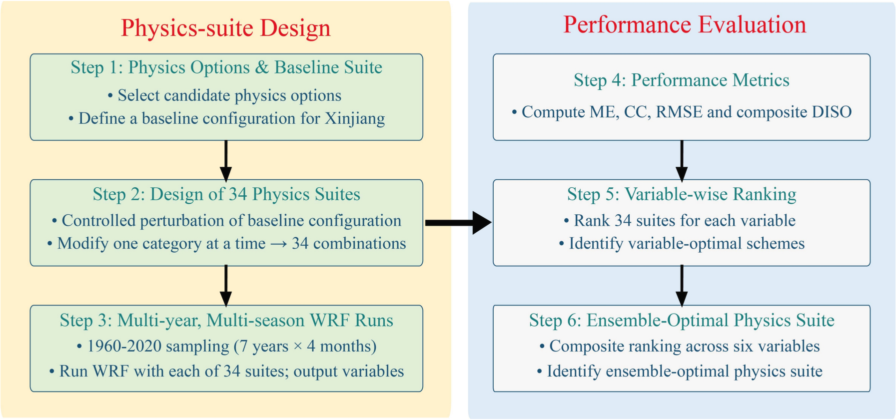

Figure 3. Conceptual framework of WRF physics evaluation in arid Xinjiang.

https://doi.org/10.5194/egusphere-2025-6248
Preprint. Discussion started: 31 March 2026

Table 1. Physical parameterization schemes used in this study

Cloud microphysics	Cumulus convection	Longwave radiation	Shortwave radiation	Planetary boundary layer	Surface layer	Land surface model
Thompson Morrison2-moment WSM6 WSM3 Lin WSM5 WDM6 NSSL 2-moment	Kain-Fritsch (new Eta) Grell-Freita Grell-3 BMJ Grell-Devenyi (GD) Multiscale Kain–Fritsch SAS Tiedtke	RRTM CAM RRTMG GFDL Goddard	Dudhia Goddard shortwave CAM RRTMG Goddard FLG (UCLA) GFDL	GBM ACM MYJ YSU MYNN BouLac UW	Revised MM5	Noah-MP Thermal Diffusion (TD) Noah-LSM CLM4

Notes: Abbreviation expansions are available in the Supplementary Material.

https://doi.org/10.5194/egusphere-2025-6248
Preprint. Discussion started: 31 March 2026

Table 2. Physics-suite combinations used in sensitivity experiments

Number	Cloud microphysics	Cumulus convection	Longwave radiation	Shortwave radiation	Planetary boundary layer	Surface layer	Land surface model
1	Thompson	Kain-Fritsch (new Eta)	RRTM	Dudhia	GBM	Revised MM5	Noah-MP
2	Thompson	Kain-Fritsch (new Eta)	CAM	Dudhia	GBM	Revised MM5	Noah-MP
3	Thompson	Kain-Fritsch (new Eta)	RRTMG	Dudhia	GBM	Revised MM5	Noah-MP
4	Thompson	Kain-Fritsch (new Eta)	GFDL	Dudhia	GBM	Revised MM5	Noah-MP
5	Thompson	Kain-Fritsch (new Eta)	Goddard	Dudhia	GBM	Revised MM5	Noah-MP
6	Thompson	Kain-Fritsch (new Eta)	RRTM	Goddard shortwave	GBM	Revised MM5	Noah-MP
7	Thompson	Kain-Fritsch (new Eta)	RRTM	CAM	GBM	Revised MM5	Noah-MP
8	Thompson	Kain-Fritsch (new Eta)	RRTM	RRTMG	GBM	Revised MM5	Noah-MP
9	Thompson	Kain-Fritsch (new Eta)	RRTM	Goddard	GBM	Revised MM5	Noah-MP
10	Thompson	Kain-Fritsch (new Eta)	RRTM	FLG (UCLA)	GBM	Revised MM5	Noah-MP
11	Thompson	Kain-Fritsch (new Eta)	RRTM	GFDL	GBM	Revised MM5	Noah-MP

12	Thompson	Kain-Fritsch (new Eta)	RRTM	Dudhia	GBM	Revised MM5	Thermal Diffusion (TD)
13	Thompson	Kain-Fritsch (new Eta)	RRTM	Dudhia	GBM	Revised MM5	Noah-LSM
14	Thompson	Kain-Fritsch (new Eta)	RRTM	Dudhia	GBM	Revised MM5	CLM4
15	Thompson	Kain-Fritsch (new Eta)	RRTM	Dudhia	ACM	Revised MM5	Noah-MP
16	Thompson	Kain-Fritsch (new Eta)	RRTM	Dudhia	MYJ	Revised MM5	Noah-MP
17	Thompson	Kain-Fritsch (new Eta)	RRTM	Dudhia	YSU	Revised MM5	Noah-MP
18	Thompson	Kain-Fritsch (new Eta)	RRTM	Dudhia	MYNN	Revised MM5	Noah-MP
19	Thompson	Kain-Fritsch (new Eta)	RRTM	Dudhia	BouLac	Revised MM5	Noah-MP
20	Thompson	Kain-Fritsch (new Eta)	RRTM	Dudhia	UW	Revised MM5	Noah-MP
21	Thompson	Grell-Freita	RRTM	Dudhia	GBM	Revised MM5	Noah-MP
22	Thompson	Grell-3	RRTM	Dudhia	GBM	Revised MM5	Noah-MP
23	Thompson	BMJ	RRTM	Dudhia	GBM	Revised MM5	Noah-MP
24	Thompson	Grell-Devenyi (GD)	RRTM	Dudhia	GBM	Revised MM5	Noah-MP
25	Thompson	Multiscale Kain–Fritsch	RRTM	Dudhia	GBM	Revised MM5	Noah-MP

26	Thompson	SAS	RRTM	Dudhia	GBM	Revised MM5	Noah-MP
27	Thompson	Tiedtke	RRTM	Dudhia	GBM	Revised MM5	Noah-MP
28	Morrison 2-moment	Kain-Fritsch (new Eta)	RRTM	Dudhia	GBM	Revised MM5	Noah-MP
29	WSM6	Kain-Fritsch (new Eta)	RRTM	Dudhia	GBM	Revised MM5	Noah-MP
30	WSM3	Kain-Fritsch (new Eta)	RRTM	Dudhia	GBM	Revised MM5	Noah-MP
31	Lin	Kain-Fritsch (new Eta)	RRTM	Dudhia	GBM	Revised MM5	Noah-MP
32	WSM5	Kain-Fritsch (new Eta)	RRTM	Dudhia	GBM	Revised MM5	Noah-MP
33	WDM6	Kain-Fritsch (new Eta)	RRTM	Dudhia	GBM	Revised MM5	Noah-MP
34	NSSL 2-moment	Kain-Fritsch (new Eta)	RRTM	Dudhia	GBM	Revised MM5	Noah-MP

Notes: Abbreviation expansions are available in the Supplementary Material.

3. Results

3.1 Adaptability of physical parameterization schemes

Physics choices exert distinct and sizable impacts on 2 m air temperature (Tav). Among microphysics schemes (Schemes 1 and 28–34), Lin (Scheme 31) yields consistently high correlation ($CC > 0.98$) and small bias ($NME \approx 0.012$). Its long-term performance ($DISO = 0.495$; rank 8) indicates good adaptability under Xinjiang's complex terrain and radiative forcing (Figs. 4–5). WSM5 (Scheme 32) is comparable but slightly more biased ($NME \approx 0.048$), whereas WSM3 (Scheme 30) performs worse ($DISO = 0.507$; rank 24), implying limited stability. For cumulus schemes (Schemes 1, 21–27), Grell–Freitas (Scheme 21) performs best ($DISO = 0.482$; rank 2) with strong CC and moderate NRMSE (0.415); the Multiscale Kain–Fritsch scheme (MSKF, Scheme 25) is close behind ($DISO = 0.488$; rank 3). Kain–Fritsch (new Eta) is weaker across metrics, suggesting limited suitability for multi-decadal climate runs. Radiation differences (Schemes 1–11) are pronounced. For longwave radiation, CAM and RRTMG perform similarly; when coupled with Dudhia shortwave radiation, CAM/Dudhia (Scheme 2; $DISO = 0.492$; rank 6) and RRTMG/Dudhia (Scheme 3; $DISO = 0.494$; rank 7) outperform other pairings. Shortwave spread is larger: Dudhia is the most stable option, whereas FLG (UCLA; Scheme 10) is markedly poor ($CC = 0.878$; $NME = -1.798$; $NRMSE = 0.959$; $DISO = 2.062$). For the planetary boundary layer (PBL; Schemes 1, 15–20), MYNN (Scheme 18) performs best ($DISO = 0.496$; rank 9; $CC \approx 0.979$; $NME \approx 0.041$), while MYJ (Scheme 16) is weakest ($DISO = 0.544$; rank 26), likely reflecting deficiencies in surface–atmosphere energy exchange. Among land-surface models (LSMs; Schemes 1, 12–14), CLM4 (Scheme 14) clearly leads ($DISO = 0.476$; rank 1), outperforming Noah-MP, Noah-LSM, and TD.

https://doi.org/10.5194/egusphere-2025-6248
Preprint. Discussion started: 31 March 2026

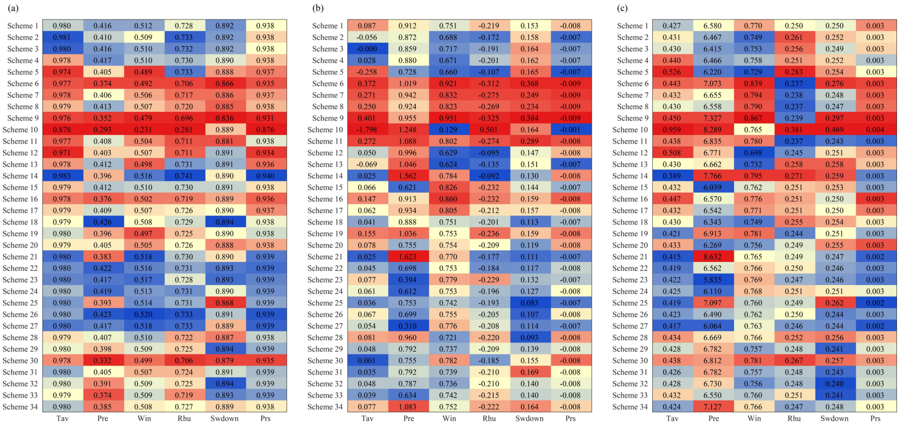

(a)

	Tav	Pre	Win	Rhu	Swdown	Prs
Scheme 1	0.980	0.416	0.512	0.728	0.892	0.938
Scheme 2	0.981	0.410	0.509	0.733	0.892	0.938
Scheme 3	0.980	0.416	0.510	0.732	0.892	0.938
Scheme 4	0.978	0.417	0.510	0.730	0.890	0.938
Scheme 5	0.974	0.405	0.489	0.733	0.888	0.937
Scheme 6	0.977	0.374	0.492	0.706	0.866	0.935
Scheme 7	0.978	0.406	0.506	0.717	0.886	0.937
Scheme 8	0.979	0.413	0.507	0.720	0.885	0.938
Scheme 9	0.976	0.352	0.479	0.696	0.836	0.931
Scheme 10	0.878	0.293	0.231	0.281	0.889	0.876
Scheme 11	0.977	0.408	0.504	0.711	0.881	0.938
Scheme 12	0.971	0.403	0.507	0.711	0.891	0.934
Scheme 13	0.978	0.412	0.498	0.731	0.891	0.936
Scheme 14	0.983	0.396	0.516	0.741	0.890	0.940
Scheme 15	0.979	0.412	0.510	0.730	0.891	0.938
Scheme 16	0.978	0.376	0.502	0.719	0.889	0.936
Scheme 17	0.979	0.409	0.507	0.726	0.890	0.937
Scheme 18	0.979	0.426	0.508	0.729	0.894	0.938
Scheme 19	0.980	0.396	0.497	0.725	0.890	0.938
Scheme 20	0.979	0.405	0.505	0.726	0.888	0.938
Scheme 21	0.980	0.383	0.518	0.730	0.890	0.939
Scheme 22	0.980	0.422	0.516	0.731	0.893	0.939
Scheme 23	0.980	0.417	0.517	0.728	0.893	0.939
Scheme 24	0.980	0.419	0.513	0.731	0.890	0.939
Scheme 25	0.980	0.393	0.514	0.731	0.868	0.939
Scheme 26	0.980	0.423	0.520	0.733	0.891	0.939
Scheme 27	0.980	0.417	0.518	0.733	0.889	0.939
Scheme 28	0.979	0.407	0.510	0.722	0.887	0.938
Scheme 29	0.980	0.398	0.509	0.725	0.894	0.939
Scheme 30	0.978	0.332	0.499	0.706	0.879	0.935
Scheme 31	0.980	0.405	0.507	0.724	0.891	0.939
Scheme 32	0.980	0.391	0.509	0.725	0.894	0.939
Scheme 33	0.979	0.374	0.509	0.719	0.893	0.939
Scheme 34	0.980	0.385	0.508	0.727	0.889	0.938

(b)

	Tav	Pre	Win	Rhu	Swdown	Prs
Scheme 1	0.087	0.912	0.751	-0.219	0.153	-0.008
Scheme 2	-0.056	0.872	0.688	-0.172	0.158	-0.007
Scheme 3	-0.000	0.859	0.717	-0.191	0.164	-0.007
Scheme 4	0.028	0.880	0.671	-0.201	0.162	-0.007
Scheme 5	-0.258	0.728	0.660	-0.107	0.165	-0.007
Scheme 6	0.372	1.019	0.921	-0.312	0.368	-0.009
Scheme 7	0.271	0.942	0.832	-0.275	0.249	-0.009
Scheme 8	0.250	0.924	0.823	-0.269	0.234	-0.009
Scheme 9	0.401	0.955	0.951	-0.325	0.384	-0.009
Scheme 10	-1.798	1.248	0.129	0.501	0.164	-0.001
Scheme 11	0.272	1.088	0.802	-0.274	0.289	-0.008
Scheme 12	0.050	0.996	0.629	-0.095	0.147	-0.008
Scheme 13	-0.069	1.046	0.624	-0.135	0.151	-0.007
Scheme 14	0.025	1.562	0.784	-0.092	0.130	-0.008
Scheme 15	0.066	0.621	0.826	-0.232	0.144	-0.007
Scheme 16	0.147	0.913	0.860	-0.232	0.159	-0.008
Scheme 17	0.062	0.934	0.805	-0.212	0.157	-0.008
Scheme 18	0.041	0.888	0.751	-0.201	0.113	-0.007
Scheme 19	0.155	1.036	0.753	-0.236	0.159	-0.008
Scheme 20	0.078	0.755	0.754	-0.209	0.119	-0.008
Scheme 21	0.025	1.623	0.770	-0.177	0.111	-0.007
Scheme 22	0.045	0.698	0.753	-0.184	0.117	-0.008
Scheme 23	0.077	0.394	0.779	-0.229	0.132	-0.007
Scheme 24	0.061	0.612	0.753	-0.196	0.127	-0.008
Scheme 25	0.036	0.753	0.742	-0.193	0.083	-0.007
Scheme 26	0.067	0.699	0.755	-0.205	0.107	-0.008
Scheme 27	0.054	0.310	0.776	-0.208	0.114	-0.007
Scheme 28	0.081	0.960	0.721	-0.220	0.093	-0.008
Scheme 29	0.048	0.792	0.737	-0.209	0.139	-0.008
Scheme 30	0.001	0.755	0.782	-0.185	0.155	-0.008
Scheme 31	0.035	0.792	0.739	-0.210	0.169	-0.008
Scheme 32	0.048	0.787	0.736	-0.210	0.140	-0.008
Scheme 33	0.039	0.634	0.742	-0.215	0.140	-0.008
Scheme 34	0.077	1.083	0.752	-0.222	0.164	-0.008

(c)

	Tav	Pre	Win	Rhu	Swdown	Prs
Scheme 1	0.427	6.580	0.770	0.250	0.250	0.003
Scheme 2	0.431	6.467	0.749	0.261	0.252	0.003
Scheme 3	0.430	6.415	0.753	0.256	0.249	0.003
Scheme 4	0.440	6.466	0.758	0.251	0.252	0.003
Scheme 5	0.526	6.220	0.729	0.283	0.254	0.003
Scheme 6	0.443	7.073	0.839	0.237	0.276	0.003
Scheme 7	0.432	6.655	0.794	0.238	0.248	0.003
Scheme 8	0.430	6.558	0.790	0.237	0.247	0.003
Scheme 9	0.450	7.327	0.867	0.239	0.297	0.003
Scheme 10	0.959	8.289	0.765	0.381	0.469	0.004
Scheme 11	0.438	6.835	0.780	0.237	0.243	0.003
Scheme 12	0.508	6.771	0.698	0.245	0.251	0.003
Scheme 13	0.430	6.662	0.732	0.258	0.258	0.003
Scheme 14	0.389	7.766	0.795	0.271	0.259	0.003
Scheme 15	0.432	6.039	0.762	0.251	0.253	0.003
Scheme 16	0.447	6.570	0.776	0.251	0.250	0.003
Scheme 17	0.432	6.542	0.771	0.251	0.250	0.003
Scheme 18	0.430	6.343	0.749	0.255	0.254	0.003
Scheme 19	0.421	6.913	0.781	0.244	0.251	0.003
Scheme 20	0.433	6.269	0.756	0.249	0.255	0.003
Scheme 21	0.415	8.632	0.765	0.249	0.247	0.002
Scheme 22	0.419	6.562	0.766	0.250	0.246	0.003
Scheme 23	0.422	5.835	0.769	0.247	0.246	0.003
Scheme 24	0.425	6.110	0.768	0.251	0.251	0.003
Scheme 25	0.419	7.097	0.760	0.249	0.262	0.002
Scheme 26	0.423	6.490	0.762	0.250	0.244	0.003
Scheme 27	0.417	6.064	0.763	0.246	0.244	0.002
Scheme 28	0.434	6.669	0.766	0.252	0.256	0.003
Scheme 29	0.428	6.782	0.757	0.248	0.241	0.003
Scheme 30	0.438	6.812	0.781	0.267	0.257	0.003
Scheme 31	0.426	6.782	0.757	0.248	0.243	0.003
Scheme 32	0.428	6.730	0.756	0.248	0.240	0.003
Scheme 33	0.432	6.550	0.760	0.251	0.241	0.003
Scheme 34	0.424	7.127	0.766	0.247	0.248	0.003

Figure 4. Performance of the 34 WRF physics suites for near-surface variables over Xinjiang. Panels (a–c) show CC, NME, and NRMSE, respectively, for six variables (Tav, Pre, Win, Rhu, Swdown, Prs).

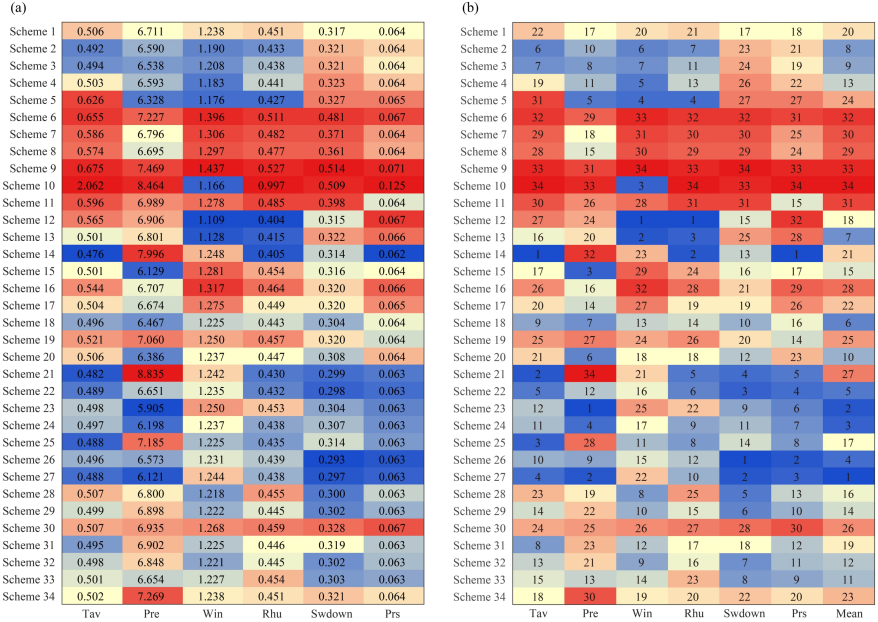

(a)

	Tav	Pre	Win	Rhu	Swdown	Prs
Scheme 1	0.506	6.711	1.238	0.451	0.317	0.064
Scheme 2	0.492	6.590	1.190	0.433	0.321	0.064
Scheme 3	0.494	6.538	1.208	0.438	0.321	0.064
Scheme 4	0.503	6.593	1.183	0.441	0.323	0.064
Scheme 5	0.626	6.328	1.176	0.427	0.327	0.065
Scheme 6	0.655	7.227	1.396	0.511	0.481	0.067
Scheme 7	0.586	6.796	1.306	0.482	0.371	0.064
Scheme 8	0.574	6.695	1.297	0.477	0.361	0.064
Scheme 9	0.675	7.469	1.437	0.527	0.514	0.071
Scheme 10	2.062	8.464	1.166	0.997	0.509	0.125
Scheme 11	0.596	6.989	1.278	0.485	0.398	0.064
Scheme 12	0.565	6.906	1.109	0.404	0.315	0.067
Scheme 13	0.501	6.801	1.128	0.415	0.322	0.066
Scheme 14	0.476	7.996	1.248	0.405	0.314	0.062
Scheme 15	0.501	6.129	1.281	0.454	0.316	0.064
Scheme 16	0.544	6.707	1.317	0.464	0.320	0.066
Scheme 17	0.504	6.674	1.275	0.449	0.320	0.065
Scheme 18	0.496	6.467	1.225	0.443	0.304	0.064
Scheme 19	0.521	7.060	1.250	0.457	0.320	0.064
Scheme 20	0.506	6.386	1.237	0.447	0.308	0.064
Scheme 21	0.482	8.835	1.242	0.430	0.299	0.063
Scheme 22	0.489	6.651	1.235	0.432	0.298	0.063
Scheme 23	0.498	5.905	1.250	0.453	0.304	0.063
Scheme 24	0.497	6.198	1.237	0.438	0.307	0.063
Scheme 25	0.488	7.185	1.225	0.435	0.314	0.063
Scheme 26	0.496	6.573	1.231	0.439	0.293	0.063
Scheme 27	0.488	6.121	1.244	0.438	0.297	0.063
Scheme 28	0.507	6.800	1.218	0.455	0.300	0.063
Scheme 29	0.499	6.898	1.222	0.445	0.302	0.063
Scheme 30	0.507	6.935	1.268	0.459	0.328	0.067
Scheme 31	0.495	6.902	1.225	0.446	0.319	0.063
Scheme 32	0.498	6.848	1.221	0.445	0.302	0.063
Scheme 33	0.501	6.654	1.227	0.454	0.303	0.063
Scheme 34	0.502	7.269	1.238	0.451	0.321	0.064

(b)

	Tav	Pre	Win	Rhu	Swdown	Prs	Mean
Scheme 1	22	17	20	21	17	18	20
Scheme 2	6	10	6	7	23	21	8
Scheme 3	7	8	7	11	24	19	9
Scheme 4	19	11	5	13	26	22	13
Scheme 5	31	5	4	4	27	27	24
Scheme 6	32	29	33	32	32	31	32
Scheme 7	29	18	31	30	30	25	30
Scheme 8	28	15	30	29	29	24	29
Scheme 9	33	31	34	33	34	33	33
Scheme 10	34	33	3	34	33	34	34
Scheme 11	30	26	28	31	31	15	31
Scheme 12	27	24	1	1	15	32	18
Scheme 13	16	20	2	3	25	28	7
Scheme 14	1	32	23	2	13	1	21
Scheme 15	17	3	29	24	16	17	15
Scheme 16	26	16	32	28	21	29	28
Scheme 17	20	14	27	19	19	26	22
Scheme 18	9	7	13	14	10	16	6
Scheme 19	25	27	24	26	20	14	25
Scheme 20	21	6	18	18	12	23	10
Scheme 21	2	34	21	5	4	5	27
Scheme 22	5	12	16	6	3	4	5
Scheme 23	12	1	25	22	9	6	2
Scheme 24	11	4	17	9	11	7	3
Scheme 25	3	28	11	8	14	8	17
Scheme 26	10	9	15	12	1	2	4
Scheme 27	4	2	22	10	2	3	1
Scheme 28	23	19	8	25	5	13	16
Scheme 29	14	22	10	15	6	10	14
Scheme 30	24	25	26	27	28	30	26
Scheme 31	8	23	12	17	18	12	19
Scheme 32	13	21	9	16	7	11	12
Scheme 33	15	13	14	23	8	9	11
Scheme 34	18	30	19	20	22	20	23

Figure 5. DISO-based comprehensive performance and ranks for the 34 suites. Panel (a) shows DISO values, and panel (b) shows standardized ranks for the six variables (Tav, Pre, Win, Rhu, Swdown, Prs); the final column in (b) indicates the mean standardized rank (overall performance).

Precipitation (Pre) is highly sensitive to physics choice, with large spread across suites (Figs. 4–5). In microphysics, WDM6 (Scheme 33) performs relatively well (DISO = 6.654; rank 13) but with modest CC (0.374). Thompson microphysics achieves higher CC (0.416) but larger overall errors (DISO = 6.711; rank 17). Cumulus schemes dominate the spread: BMJ (Scheme 23) is best overall (DISO = 5.905; rank 2), followed by Tiedtke and Grell–Dévényi (GD) (DISO = 6.121 and 6.198). Grell–Freitas (Scheme 21) is weakest (DISO = 8.835; rank 34). Radiation

https://doi.org/10.5194/egusphere-2025-6248
Preprint. Discussion started: 31 March 2026

effects are also substantial: Goddard/Dudhia (Scheme 5) performs best (DISO = 6.328; rank 5), followed by RRTMG/Dudhia (DISO = 6.538; rank 8); RRTM/FLG (UCLA; Scheme 10) is poorest (DISO = 8.464; rank 33). Longwave Goddard and RRTMG outperform RRTM, while shortwave RRTMG, Dudhia, and CAM are robust; Goddard shortwave and FLG are weak. LSM effects are smaller: Noah-MP (Scheme 1) is best (DISO = 6.711; rank 17), whereas CLM4 (Scheme 14) performs notably worse for precipitation (DISO = 7.996; rank 32).

For 10 m wind speed (Win), performance is controlled primarily by PBL and surface processes. In microphysics, Morrison 2-moment (Scheme 28) is best (DISO = 1.218; rank 8), with WSM5, WSM6, Lin, and WDM6 giving similar results (DISO = 1.221–1.227). WSM3 (Scheme 30) is poorest (DISO = 1.268; rank 26) (Figs. 4–5). Among cumulus schemes, MSKF (Scheme 25) performs best (DISO = 1.225; rank 11), while BMJ (Scheme 23) is weakest (DISO = 1.250; rank 25). For radiation (Schemes 1–11), RRTM/FLG (Scheme 10) yields the smallest DISO (1.166; rank 3); Goddard/Dudhia, GFDL/Dudhia, CAM/Dudhia, and RRTMG/Dudhia (Schemes 2–5) also perform well (DISO = 1.176–1.208; ranks 4–7), whereas RRTM/Goddard (Scheme 9) is weakest (DISO = 1.437; rank 34). Longwave Goddard generally outperforms RRTM, and shortwave FLG is superior to Goddard shortwave for wind. For the PBL, MYNN (Scheme 18) again leads (DISO = 1.225; rank 13), followed by UW and GBM (DISO = 1.237 and 1.238; ranks 18 and 20); MYJ (Scheme 16) is weaker (DISO = 1.317; rank 32). For LSMs, TD and Noah-LSM are best (DISO = 1.109 and 1.128; ranks 1 and 2), whereas Noah-MP and CLM4 are relatively poor (DISO = 1.238 and 1.248; ranks 20 and 23).

Relative humidity (Rhu) is jointly controlled by microphysics, convection, PBL mixing, and land–atmosphere exchange (Figs. 4–5). Microphysics differences are modest (DISO = 0.445–0.458), with WSM6 (Scheme 29) slightly better (DISO = 0.445; rank 15). Cumulus differences are larger: Grell–Freitas (Scheme 21) performs best (DISO = 0.430; rank 5), followed by Grell-3 (Scheme 22; DISO = 0.432; rank 6), whereas BMJ (Scheme 23) is weakest (DISO = 0.453; rank 22). Radiation influence is strong: RRTMG/Dudhia (Scheme 5) ranks first (DISO = 0.427; rank 4), with GFDL/Dudhia (Scheme 2) close behind (DISO = 0.433; rank 7). Schemes 6–11 are generally poor, with RRTM/FLG (UCLA; Scheme 10) the worst (DISO = 0.997; rank 34). Longwave Goddard generally outperforms RRTM, and shortwave Dudhia outperforms FLG. For the PBL, MYNN (Scheme 18) is most accurate (DISO = 0.443; rank 14), followed by UW and YSU (DISO = 0.446 and 0.449; ranks 18–19); MYJ (Scheme 16) is weakest (DISO = 0.464; rank 28). For LSMs, TD and CLM4 are best (DISO = 0.404 and 0.405; ranks 1–2), while Noah-MP (Scheme 1) performs worse (DISO = 0.451; rank 21).

Surface downward shortwave radiation (Swdown) is highly sensitive to both microphysics and radiation. Among microphysics schemes (Schemes 28–34), Morrison 2-moment (Scheme 28) performs best (DISO = 0.300; rank 5); WSM6, WSM5, and WDM6 are similar (DISO ≈ 0.302), while WSM3 (Scheme 30) is weaker (DISO = 0.328; rank 28) (Figs. 4–5). For cumulus schemes, SAS (Scheme 26) ranks first (DISO = 0.293; rank 1), followed by Tiedtke (DISO = 0.297) and Grell-3 (DISO = 0.298), whereas Kain–Fritsch (new Eta) is weaker (DISO = 0.317; rank 17). Radiation spread is largest: RRTM/Dudhia performs best (DISO = 0.316), with CAM/Dudhia and RRTMG/Dudhia next (DISO = 0.321 each). RRTM/Goddard (Scheme 9) and RRTM/FLG (Scheme 10) are poorest (DISO > 0.5). Longwave RRTM is generally better than Goddard, and shortwave Dudhia is better than Goddard shortwave. For the PBL, MYNN (Scheme 18) performs best (DISO = 0.304; rank 10), while MYJ (Scheme 16) and BouLac (Scheme 19) are weaker (DISO = 0.320; ranks 20–21). Among LSMs, CLM4 (Scheme 14) leads (DISO = 0.314; rank 1), whereas Noah-LSM (Scheme 13) is more biased (DISO = 0.322; rank 25).

Surface pressure (Prs) shows distinct but generally small sensitivities. For microphysics, WDM6 (Scheme 33) is best (DISO = 0.063), whereas WSM3 (Scheme 30) is poorer (DISO = 0.067) (Figs. 4–5). For cumulus, SAS (Scheme 26) is most accurate (DISO = 0.063), followed by Kain–Fritsch (new Eta) (DISO = 0.064). Shortwave choice has limited impact (typical DISO 0.064–0.065), whereas longwave differences are more evident, with Goddard and FLG (UCLA) unsuitable. LSMs matter: CLM4 (Scheme 14) is strongest (DISO = 0.062), while TD is weakest (DISO = 0.067).

3.2 Single-variable and multi-variable optimization

Temporal evolution of Tav is well captured (CC > 0.97 for most suites), but error magnitudes vary. Most suites exhibit a warm bias. Schemes 3 and 30 show minimal bias, while Scheme 10 is cold-biased. Overall, Scheme 14 (CLM4) performs best (CC = 0.983; NRMSE = 0.389; DISO = 0.476), followed by Schemes 21, 25, and 27; Scheme 10 is weakest (Figs. 4–5). For precipitation, skill remains limited, with a mean CC of 0.397 and systematic overestimation (mean NME = 0.884) (Fig. 4). Schemes 27 and 23 feature the smallest biases, whereas Scheme 21 exhibits the largest. NRMSE spread is large; Scheme 23 (BMJ) is most accurate overall and ranks first by DISO (5.905), followed by Schemes 27 and 15 (Fig. 5).

The temporal evolution of wind speed is represented with moderate skill (typical CC ≈ 0.5). Scheme 26 ranks best by CC, whereas Scheme 10 is weakest (Fig. 4). All suites overestimate wind speed (mean NME = 0.743). Scheme 10 exhibits the smallest bias and Scheme 9 the largest. By NRMSE, Scheme 12 is most accurate (0.698) and Scheme 9 least (0.867). The composite DISO highlights Schemes 12 and 13 as most balanced (1.109 and 1.128), while the weak CC of Scheme 10 limits its practical value. Schemes 6–9 are generally poor. Relative humidity evolution is reproduced with comparatively good reliability (mean CC = 0.711). Most suites have CC > 0.70 (best: Scheme 14, CC = 0.741), with Scheme 10 again an outlier (CC = 0.281). A modest dry bias prevails (mean NME = −0.187). Scheme 14 minimizes this bias (NME = −0.092), whereas Scheme 10 is worst (NME = 0.500). NRMSE averages 0.254 (best: Scheme 6, 0.237; worst: Scheme 10, 0.381). By DISO, Scheme 12 performs best (0.404), closely followed by Schemes 13 and 14; Schemes 6–10 generally perform poorly (Fig. 5).

https://doi.org/10.5194/egusphere-2025-6248
Preprint. Discussion started: 31 March 2026

Swdown is reproduced with high fidelity overall (mean CC = 0.887). Scheme 18 attains the highest CC (0.984); Scheme 9 is lowest (0.836) but still acceptable. Biases are smallest for Schemes 28 and 26 (NME = 0.093 and 0.107), whereas Schemes 9 and 6 markedly overestimate. NRMSE is smallest for Scheme 32 (0.240) and largest for Scheme 10 (0.469). By DISO (Fig. 5), Scheme 26 is most balanced (0.293), with Schemes 27, 22, and 23 close behind; Schemes 9 and 10 are poor (DISO > 0.5). Surface pressure is the most stable variable, with mean CC = 0.936 (Fig. 4). Nearly all suites achieve CC > 0.93 (best: Scheme 14, CC = 0.940; weakest: Scheme 10, CC = 0.876). A slight low bias exists overall (mean NME = −0.008), with a narrow range (−0.009 to −0.001). NRMSE is < 0.003 for almost all suites. By DISO, Scheme 14 again performs best (0.062); aside from Schemes 9 and 10, all suites have DISO < 0.067.

3.3 Spatiotemporal reproduction under variable-optimal suites

Temperature (Scheme 14). Seasonal cycles are well captured with small biases (spring −0.26°C; autumn 0.45°C; summer 0.93°C; winter 1.46°C). Spatial skill is high (mean CC = 0.983; >94% of stations CC > 0.97). Overestimation concentrates along the southern Tianshan foothills (e.g., Baicheng, Turpan Eastkan, Hoxud); underestimation appears at high elevations (e.g., Tianchi, Baluntai). NRMSE and DISO maps align, with smaller errors over southern Xinjiang and weaker skill in northern mountains and the eastern Tianshan (Fig. 6; Fig. S1).

Precipitation (Scheme 23). The seasonal cycle is reproduced but with systematic overestimation. Biases are larger in spring (0.22 mm) and summer (0.27 mm) than autumn (0.15 mm) and winter (0.09 mm). Spatially, skill is higher in the north (CC = 0.499) than the south (CC = 0.338), with better performance in Tianshan and weaker skill in southern basins (Fig. S2). ME/RMSE show a north–south gradient (north: 0.328 mm and 2.738 mm; south: 0.086 mm and 1.370 mm). Despite larger mean errors in the north, stronger temporal coherence yields better integrated performance (DISO = 3.643 vs. 8.080). Overall, precipitation remains intrinsically challenging under Xinjiang's arid, complex terrain.

Wind speed (Scheme 12). Temporal evolution is captured but with persistent overestimation. Bias is smallest in winter (ME = 0.89 m s^{-1}) and largest in spring–autumn (1.12–1.30 m s^{-1}). Spatial skill is moderate (mean CC = 0.507), higher along the northern Tianshan slopes and lower in western/southern basins (Fig. S3). Overestimation occurs at ~95% of stations, larger in the south (ME = 1.611 m s^{-1}) than the north (0.655 m s^{-1}); extremes (>3 m s^{-1}) occur at Tashkurgan and Yingjisha. RMSE is smaller in basins than high terrain, with the largest deviations over western Xinjiang and eastern Tianshan. DISO confirms better performance in the north (higher CC, smaller errors) and weaker skill in southern basins.

Relative humidity (Scheme 12). Seasonality is well reproduced but with warm-season dry bias (winter ME = −0.29%; spring −1.96%; autumn −10.12%; summer −7.60%). Spatial skill is moderate (mean CC = 0.711), weaker in the south. Underestimation occurs at ~85% of stations, especially the western Tarim (e.g., Baicheng > 20%); errors are <4% at many northern Tianshan sites. RMSE averages 12.76%, larger at Tianchi (16.51%) and Daxigou (16.23%) (Fig. S4). DISO shows stronger performance in the north (0.354) than south (0.451), with high-error zones in southern basins (e.g., Tashkurgan, Moyu) and some mountain areas (e.g., Bayanbulak, Baluntai).

Shortwave radiation (Scheme 26). Skill peaks in autumn–winter, with slight winter underestimation (ME = −0.04 MJ m^{-2} day^{-1}) and warm-season overestimation (spring 3.23; summer 2.93). Spatial correlations are high overall (CC = 0.891), higher in the north (0.926) than south (0.863), and lowest in the southwest (e.g., Hotan, CC ≈ 0.76) (Fig. S5).

Surface pressure (Scheme 14). Pressure shows the highest spatial coherence and stability. Seasonal variations are reproduced with small low bias (summer −0.75 kPa; others −0.61 to −0.65 kPa). Spatially, skill is higher in southern Xinjiang (CC = 0.957) than the north (0.921); weaker agreement occurs near Wenquan, Fuyun, and Urumqi (Fig. S6). ME/RMSE/DISO maps are consistent, indicating reduced skill over the Tianshan and northern regions but overall high accuracy.

3.4 Ensemble-optimal suite

A composite ranking based on standardized DISO for the six variables identifies Scheme 27, Thompson microphysics, Tiedtke cumulus, RRTM (longwave) and Dudhia (shortwave) radiation, GBM PBL, Revised MM5 surface layer, and Noah-MP LSM, as the most robust cross-variable configuration (Fig. 4b). It ranks within the top five for Tav, Pre, Swdown, and Prs, indicating strong cross-process adaptability; its lower rank for Win (22nd) reflects trade-offs in boundary-layer representation. Time series (Fig. 6) show that the ensemble-optimal suite reproduces multi-variable variability as well as, or better than, the single-variable optima, and spatial diagnostics (Fig. 7) confirm comparable or superior performance across Xinjiang. Despite some degradation in the most complex terrain, the suite remains stable and credible region wide. We therefore recommend Scheme 27 as an ensemble-optimal configuration for constructing high-resolution meteorological datasets and for subsequent climate-change applications in Xinjiang.

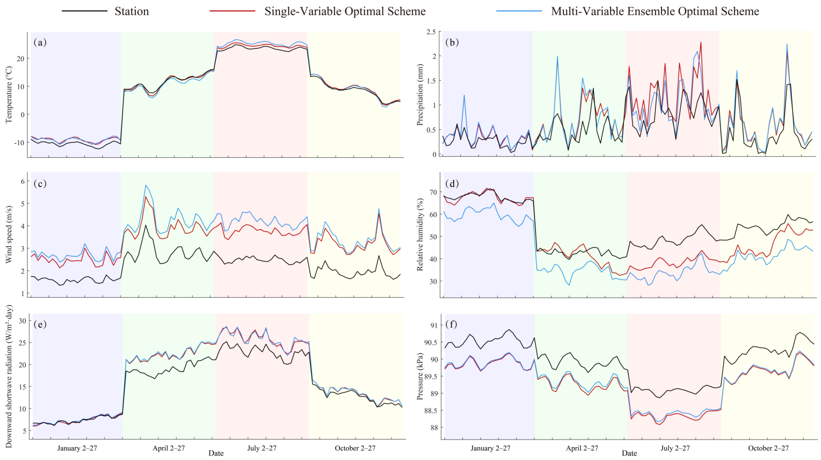

Figure 6. Seasonal evolution of simulated and observed variables under variable-optimal suites (red) and the ensemble-optimal suite (blue); observations are shown in black. Shading indicates seasons: spring (green), summer (orange), autumn (yellow), and winter (purple).

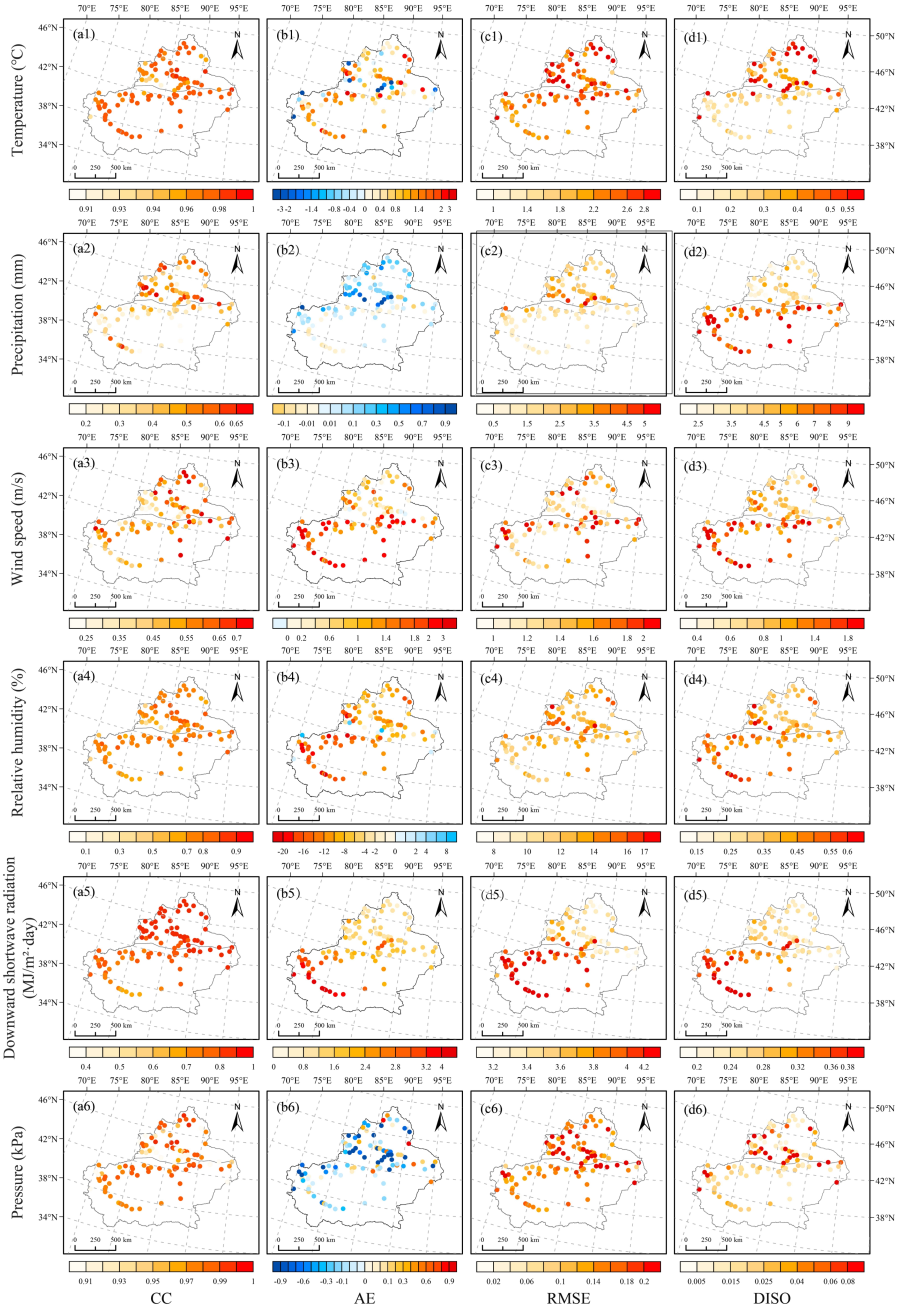

Figure 7. Spatial maps of CC, ME, RMSE, and DISO for temperature, precipitation, wind speed, relative humidity, Swdown, and surface pressure under the ensemble-optimal suite.

https://doi.org/10.5194/egusphere-2025-6248
Preprint. Discussion started: 31 March 2026

4. Discussion

4.1 Mechanisms underlying variable-specific performance

The 61-year evaluation (1960–2020) reveals systematic contrasts in WRF skill across near-surface variables, reflecting how physical processes interact with Xinjiang's arid, mountainous environment. Variables primarily regulated by large-scale dynamics and radiative balance, Tav and Prs, display high skill (CC > 0.9), strong spatial coherence, and weak sensitivity to subgrid physics. Their robustness over complex terrain is consistent with findings from Europe, the Tibetan Plateau, and the Loess Plateau (Garcia-Diez et al., 2015; Gao et al., 2015; Tian et al., 2022). In contrast, Pre exhibits the largest uncertainty, driven by the combined effects of orography and parameterization limitations. Simplified condensate/ice-phase treatments in several microphysics schemes can amplify latent-heating errors and enhance condensate production (Thompson and Eidhammer, 2014; Guo et al., 2019). Cumulus schemes such as Kain–Fritsch and Grell–Freitas tend to trigger convection too frequently in mountain–basin environments (Tianshan, Kunlun), producing systematic wet biases (Prein et al., 2013; Pennelly et al., 2014; Jeworrek et al., 2019). Additional uncertainty stems from moisture-transport errors under strong orographic forcing (Yao et al., 2021; Zhang et al., 2023a), echoing previous studies of convective events in arid regions of China (Liu et al., 2020; Zhang et al., 2023c; Van De Vyver et al., 2021).

Biases in Win, Rhu, and Swdown highlight further process-level gaps. Persistent wind overestimation arises from PBL turbulence closures and surface-drag formulations that under-dissipate momentum, particularly in basins, while orographic uplift can locally offset this bias in mountains (Pan et al., 2021; Jia et al., 2023). The warm-season dry bias in Rhu reflects insufficient evapotranspiration under low soil moisture and vigorous PBL mixing that dilutes near-surface humidity (Santanello et al., 2011; Dirmeyer, 2011; Lu et al., 2021). Overestimation of Swdown in spring–summer aligns with missing or weak aerosol–radiation and cloud–radiation interactions; dust and haze, ubiquitous in southern Xinjiang, reduce surface insolation through scattering and absorption, processes underrepresented in standard radiation options (Choobari et al., 2014).

4.2 Physical basis for scheme-dependent differences

The 34-suite comparison shows that physics selection directly controls fidelity in Pre, Win, Rhu, and Swdown. For Pre, uncertainty arises from microphysics–cumulus interplay. Thompson microphysics improves temporal coherence via refined hydrometeor phase and amount, while more complex double-moment schemes can improve latent-heat realism yet still over-produce rainfall in this regime (Thompson and Eidhammer, 2014). Cumulus physics is decisive for deep-convection timing and frequency: BMJ uses moisture-layer depth and relaxation adjustment to suppress premature triggering, yielding superior bias control in Xinjiang (Tian et al., 2021; Yang et al., 2021). In contrast, Kain–Fritsch can release convective available potential energy (CAPE) too early under moist conditions, and Grell–Freitas, despite scale awareness, tends to over-trigger over steep terrain, explaining contrasting precipitation biases in arid, topographically complex settings (Prein et al., 2013). Near-surface wind and humidity biases primarily reflect PBL–LSM coupling. Win overestimation stems from inadequate turbulence representation and under-dissipation of surface momentum in many closures. MYNN and UW reduce this via prognostic TKE and improved non-local mixing, yielding more realistic boundary-layer structure (Huang and Bai, 2023). MYJ underestimates Win under stable nocturnal conditions (weak vertical mixing), whereas YSU can overpredict daytime Win via vigorous non-local exchange.

The Rhu dry bias is compounded by weak surface moisture fluxes and vertical dilution by turbulent mixing (Banks et al., 2016). In a hyper-arid setting, correct land–atmosphere coupling is critical. CLM4 performs well for Tav, Prs, and Rhu through multi-layer soil heat and moisture transfer, dynamic vegetation albedo, and canopy resistance, sustaining the delicate hydrothermal balance of arid landscapes (He et al., 2022; Sharma et al., 2024). The simplified TD LSM lacks key biogeophysical feedbacks; limited evapotranspiration plus strong PBL mixing elevates moisture aloft, strengthening the dry bias (Lu et al., 2022). This dual mechanism clarifies why Scheme 12, while statistically strong for Rhu, still shows pronounced warm-season underestimation in southern basins. Radiative biases are linked to the fidelity of aerosol–cloud optics. RRTM (LW) + Dudhia (SW) performs best overall, whereas RRTM/FLG (UCLA) and RRTM/Goddard under-represent cloud and aerosol optical properties, degrading Swdown skill (Ju et al., 2022). In spring–summer dust and haze regimes, radiation schemes lacking explicit aerosol–radiation interactions systematically overestimate surface Swdown, producing a distinct seasonal bias pattern, positive in MAM/JJA and near-realistic in SON/DJF—with generally better skill in the north (Seifert et al., 2023).

A key outcome is that no single scheme dominates across all variables and processes in arid, complex terrain. The strength of the ensemble-optimal suite (Scheme 27) derives from cross-scheme synergy rather than any single component. Tiedtke cumulus and Thompson microphysics are complementary: Tiedtke constrains total wet bias, and Thompson improves temporal coherence. RRTM/Dudhia radiation with Noah-MP provides a physically consistent energy–moisture framework. Such "balanced" suites echo ensemble findings in Europe and elsewhere (Garcia-Diez et al., 2015). Thus, enhancing regional climate skill depends on coordinated, process-level optimization across interacting schemes, rather than pushing a single module to its limit.

4.3 Limitations and future directions

Despite providing a comprehensive view of WRF applicability over Xinjiang and clarifying scheme behavior and mechanisms, several limitations remain that motivate future work. First, validation data sparsity and representativeness are an issue: station networks are thin in high mountains and southern deserts, likely underestimating biases over these surface types. A multi-source validation framework that blends higher-density in situ observations, satellite products, and reanalysis would better constrain three-dimensional fields and capture land–atmosphere diversity. Second, resolution constraints over steep terrain persist. The 10 km nest smooths fine-scale orography and boundary-layer features, biasing local circulations and thermodynamic gradients (e.g., Tianshan). Moving to kilometer-scale, convection-permitting (CPM) configurations would reduce reliance on cumulus parameterization and explicitly resolve terrain–convection coupling, improving extreme Pre and severe-wind representations. Third, several key processes remain missing or simplified: online aerosol–radiation and aerosol–microphysics coupling (including mineral dust) is needed to correct warm-season Swdown biases; more realistic soil-moisture–vegetation–ET feedbacks are required to address the Rhu dry bias in desert basins; and improved ice-phase processes and triggering criteria are needed to mitigate Pre overestimation. Progress should emphasize integrated advances across radiation, LSM, and convection, rather than isolated tuning, with priorities including online aerosol–climate coupling, refined hydrologic parameterizations in LSMs, and systematic tests against canonical Xinjiang systems (orographic precipitation, convective storms, dust–radiative feedback). Finally, because our framework targets climatological means, extremes remain only indirectly assessed. Future work should incorporate extreme-value diagnostics, multi-model and multi-scheme ensembles, and quantified uncertainty under scenario forcing to strengthen actionable guidance for water management, ecosystem protection, and risk reduction in arid mountain–basin systems.

5. Conclusion

Using 34 WRF physics-suite combinations, we systematically evaluated six near-surface variables over Xinjiang for 1960–2020 and clarified both the adaptability and limitations of key physical processes under arid, topographically complex conditions. Model skill depends strongly on governing physics: variables dominated by large-scale dynamics and radiative balance (Tav, Prs) are most robust and spatially coherent, whereas those sensitive to subgrid processes (Pre, Win, Rhu) show larger uncertainty. Pre is the least reproducible field, with a pervasive wet bias and low correlation, while Swdown exhibits high temporal coherence but pronounced spring–summer overestimation, consistent with incomplete representation of aerosol–cloud–radiation interactions.

From a process perspective, parameterization choice is decisive. Pre biases are controlled primarily by cumulus triggering: BMJ, through moist-layer depth diagnosis and relaxation adjustment, effectively suppresses premature initiation and reduces wet bias in arid regimes, whereas Thompson microphysics enhances the temporal coherence of rainfall variability. Near-surface wind and humidity biases arise mainly from PBL–LSM coupling. MYNN mitigates Win overestimation and limits vertical moisture dilution through more realistic turbulent mixing, while advanced land models such as CLM4, via detailed soil–vegetation–atmosphere coupling, improve Tav, Rhu, and Prs. These results highlight that realistic land–atmosphere exchange is central to maintaining the hydrothermal balance of drylands.

An ensemble-optimal configuration, Thompson (microphysics), Tiedtke (cumulus), RRTM/Dudhia (LW/SW radiation), GBM (PBL), Revised MM5 (surface layer), and

https://doi.org/10.5194/egusphere-2025-6248
Preprint. Discussion started: 31 March 2026

Noah-MP (LSM), emerges as the most balanced cross-variable suite. Its strength lies in complementary process interactions rather than any single dominant scheme, underscoring a key principle for arid, complex terrain: performance gains come from synergistic, cross-scheme optimization, not from isolated tuning of individual modules.

Future work should target higher fidelity in key processes and scales: (i) online coupling of aerosols with radiation and microphysics to reduce warm-season Swdown bias; (ii) refined land-surface hydrologic parameterizations to improve soil-moisture–vegetation–ET feedbacks and thereby reduce Rhu and Tav biases in desert basins; and (iii) kilometer-scale, convection-permitting simulations to explicitly resolve terrain–convection coupling and improve extremes. Building on these advances, systematic evaluation of extreme events (intense Pre, high winds, dust storms) with tailored diagnostics and ensemble frameworks will further enhance the utility of WRF for climate-change assessment and risk reduction in Xinjiang and other arid mountain–basin systems.

Code and data availability

The core daily near-surface meteorological dataset generated in this study, covering multiple WRF physics parameterization schemes over Xinjiang, is publicly available via Zenodo at https://doi.org/10.5281/zenodo.18182172 (Xu et al., 2026).

The ASTER GDEM v003 elevation data and MODIS MCD12Q1 v061 land-use/land-cover data used as static inputs are publicly available from NASA Earthdata (https://www.earthdata.nasa.gov). Other input and validation datasets are described in detail in the manuscript and the referenced data sources.

All model configuration files and custom scripts used in this study are available at https://github.com/apsiamsuer/GMD.

Author contributions

Y.X., L.Z. and Z.H. conceived the research. Y.X. and Z.H. managed the data and developed the approach for data validation. Y.X. and L.Z. completed the data analysis, and wrote the first draft of the manuscript. M.B. and S.T checked and revised the manuscript. All authors have made substantial contributions to this research.

Competing interests

The authors declare no competing interests.

Disclaimer

Financial support

This work is supported by the Strategic Priority Research Program of the Chinese Academy of Sciences (Grant No. E4GZ06040304); the National Natural Science Foundation of China (Grant No. 42305055).

References

Banks, R. F., Tiana-Alsina, J., Baldasano, J. M., Rocadenbosch, F., Papayannis, A., Solomos, S., and Tzanis, C. G.: Sensitivity of boundary-layer variables to PBL schemes in the WRF model based on surface meteorological observations, lidar, and radiosondes during the HygrA-CD campaign, Atmospheric Research, 176, 185–201, https://doi.org/10.1016/j.atmosres.2016.02.024, 2016.

Benson, D. O. and Dirmeyer, P. A.: The soil moisture–surface flux relationship as a factor for extreme heat predictability in subseasonal to seasonal forecasts, Journal of Climate, 36, 6375–6392, https://doi.org/10.1175/jcli-d-22-0447.1, 2023.

Chen, G., Lu, Y., Hua, S., Liu, Q., Zhao, K., Zheng, Y., Wang, M., Zhang, S., and Wang, X.: Evaluating the variability of simulated raindrop size distributions in the "21•7" Henan extremely heavy rainfall event, Geophysical Research Letters, 50, https://doi.org/10.1029/2023gl102849, 2023.

Choobari, O. A., Zawar-Reza, P., and Sturman, A.: The global distribution of mineral dust and its impacts on the climate system: a review, Atmospheric Research, 138, 152–165, https://doi.org/10.1016/j.atmosres.2013.11.007, 2014.

Dirmeyer, P. A.: The terrestrial segment of soil moisture–climate coupling, Geophysical Research Letters, 38, https://doi.org/10.1029/2011gl048268, 2011.

Du, H., Zhou, C., Tang, H., Jin, X., Chen, D., Jiang, P., and Li, M.: Simulation and estimation of future precipitation changes in arid regions: a case study of Xinjiang, Northwest China, Climatic Change, 167, https://doi.org/10.1007/s10584-021-03192-z, 2021.

Gao, S. B., Huang, D. L., Du, N. Z., Ren, C. Y., and Yu, H. Q.: WRF ensemble dynamical downscaling of precipitation over China using different cumulus convective schemes, Atmospheric Research, 271, https://doi.org/10.1016/j.atmosres.2022.106116, 2022.

Gao, Y., Xu, J., and Chen, D.: Evaluation of WRF mesoscale climate simulations over the Tibetan Plateau during 1979–2011, Journal of Climate, 28, 2823–2841, https://doi.org/10.1175/jcli-d-14-00300.1, 2015.

Garcia-Diez, M., Fernandez, J., and Vautard, R.: An RCM multi-physics ensemble over Europe: multi-variable evaluation to avoid error compensation, Climate Dynamics, 45, 3141–3156, https://doi.org/10.1007/s00382-015-2529-x, 2015.

Guo, Z., Fang, J., Sun, X., Yang, Y., and Tang, J.: Sensitivity of summer precipitation simulation to microphysics parameterization over Eastern China: convection-permitting regional climate simulation, Journal of Geophysical Research-Atmospheres, 124, 9183–9204, https://doi.org/10.1029/2019jd030295, 2019.

He, J., Chen, D., Gu, Y., Jia, H., Zhong, K., and Kang, Y.: Evaluation of planetary boundary layer schemes in WRF model for simulating sea-land breeze in Shanghai, China, Atmospheric Research, 278, https://doi.org/10.1016/j.atmosres.2022.106337, 2022.

Hersbach, H., Bell, B., Berrisford, P., Hirahara, S., Horanyi, A., Munoz-Sabater, J., Nicolas, J., Peubey, C., Radu, R., Schepers, D., Simmons, A., Soci, C., Abdalla, S., Abellan, X., Balsamo, G., Bechtold, P., Biavati, G., Bidlot, J., Bonavita, M., De Chiara, G., Dahlgren, P., Dee, D., Diamantakis, M., Dragani, R., Flemming, J., Forbes, R., Fuentes, M., Geer, A., Haimberger, L., Healy, S., Hogan, R. J., Holm, E., Janiskova, M., Keeley, S., Laloyaux, P., Lopez, P., Lupu, C., Radnoti, G., de Rosnay, P., Rozum, I., Vamborg, F., Villaume, S., and Thepaut, J.-N.: The ERA5 global reanalysis, Quarterly Journal of the Royal Meteorological Society, 146, 1999–2049, https://doi.org/10.1002/qj.3803, 2020.

Hobbs, W. R., Klekociuk, A. R., and Pan, Y.: Validation of reanalysis Southern Ocean atmosphere trends using sea ice data, Atmospheric Chemistry and Physics, 20, 14757–14768, https://doi.org/10.5194/acp-20-14757-2020, 2020.

Huang, L. and Bai, L.: Evaluation of planetary boundary layer schemes on the urban heat islands in the urban agglomeration over the greater bay area in South China, Frontiers in Earth Science, 10, https://doi.org/10.3389/feart.2022.1065074, 2023.

Jeworrek, J., West, G., and Stull, R.: Evaluation of cumulus and microphysics parameterizations in WRF across the convective gray zone, Weather and Forecasting, 34, 1097–1115, https://doi.org/10.1175/waf-d-18-0178.1, 2019.

Jia, W., Zhang, X., Wang, H., Wang, Y., Wang, D., Zhong, J., Zhang, W., Zhang, L., Guo, L., Lei, Y., Wang, J., Yang, Y., and Lin, Y.: Comprehensive evaluation of typical planetary boundary layer (PBL) parameterization schemes in China – Part 1: understanding expressiveness of schemes for different regions from the mechanism perspective, Geoscientific Model Development, 16, 6635–6670, https://doi.org/10.5194/gmd-16-6635-2023, 2023.

Jin, C., He, Q., and Huang, Q.: Effect of water vapor transport on a typical rainstorm process in the arid region of southern Xinjiang: observations and numerical simulations, Remote Sensing, 15, https://doi.org/10.3390/rs15164082, 2023.

Ju, C., Li, H., Li, M., Liu, Z., Ma, Y., Mamtimin, A., Sun, M., and Song, Y.: Comparison of the forecast performance of WRF using Noah and Noah-MP land surface schemes in Central Asia arid region, Atmosphere, 13, https://doi.org/10.3390/atmos13060927, 2022.

Koecher, G., Zinner, T., and Knote, C.: Influence of cloud microphysics schemes on weather model predictions of heavy precipitation, Atmospheric Chemistry and Physics, 23, 6255–6269, https://doi.org/10.5194/acp-23-6255-2023, 2023.

Li, Q., Yang, T., and Li, L.: Quantitative assessment of the parameterization sensitivity of the WRF/Noah-MP model of snow dynamics in the Tianshan Mountains, Central Asia, Atmospheric Research, 277, https://doi.org/10.1016/j.atmosres.2022.106310, 2022.

Li, Q., Yang, T., Qi, Z., and Li, L.: Spatiotemporal variation of snowfall to precipitation ratio and its implication on water resources by a regional climate model over Xinjiang, China, Water, 10, https://doi.org/10.3390/w10101463, 2018.

Li, Z., Wan, B., Duan, Z., He, Y., Yu, Y., and Chen, H.: Evaluation of HY-2C and CFOSAT satellite retrieval offshore wind energy using Weather Research and Forecasting (WRF) simulations, Remote Sensing, 15, https://doi.org/10.3390/rs15174172, 2023.

Liu, J., Fan, S., Ali, M., Li, H., Zhang, H., Wang, Y., and Aihaiti, A.: Assimilation of water vapor retrieved from radar reflectivity data through the Bayesian method, Remote Sensing, 14, https://doi.org/10.3390/rs14225897, 2022.

Liu, P., Yang, Y., Xin, Y., and Wang, C.: Impact of lightning data assimilation on forecasts of a leeward slope precipitation event in the western margin of the Junggar Basin, Remote Sensing, 13, https://doi.org/10.3390/rs13183584, 2021.

Liu, Y., Chen, X., Li, Q., Yang, J., Li, L., and Wang, T.: Impact of different microphysics and cumulus parameterizations in WRF for heavy rainfall simulations in the central segment of the Tianshan Mountains, China, Atmospheric Research, 244, https://doi.org/10.1016/j.atmosres.2020.105052, 2020.

Lu, S., Guo, W., Ge, J., and Zhang, Y.: Impacts of land surface parameterizations on simulations over the arid and semiarid regions: the case of the Loess Plateau in China, Journal of Hydrometeorology, 23, 891–907, https://doi.org/10.1175/jhm-d-21-0143.1, 2022.

Lu, S., Guo, W., Xue, Y., Huang, F., and Ge, J.: Simulation of summer climate over Central Asia shows high sensitivity to different land surface schemes in WRF, Climate Dynamics, 57, 2249–2268, https://doi.org/10.1007/s00382-021-05876-9, 2021.

Luo, C., Shang, S., Xie, Y., He, Z., Wei, G., Zhang, F., and Wang, L.: Evaluation of the effect of WRF physical parameterizations on typhoon and wave simulation in the Taiwan Strait, Water, 15, https://doi.org/10.3390/w15081526, 2023.

Pan, L., Liu, Y., Roux, G., Cheng, W., Liu, Y., Hu, J., Jin, S., Feng, S., Du, J., and Peng, L.: Seasonal variation of the surface wind forecast performance of the high-resolution WRF-RTFDDA system over China, Atmospheric Research, 259, https://doi.org/10.1016/j.atmosres.2021.105673, 2021.

Pennelly, C., Reuter, G., and Flesch, T.: Verification of the WRF model for simulating heavy precipitation in Alberta, Atmospheric Research, 135, 172–192, https://doi.org/10.1016/j.atmosres.2013.09.004, 2014.

Prein, A. F., Gobiet, A., Suklitsch, M., Truhetz, H., Awan, N. K., Keuler, K., and Georgievski, G.: Added value of convection permitting seasonal simulations, Climate Dynamics, 41, 2655–2677, https://doi.org/10.1007/s00382-013-1744-6, 2013.

Santanello, J. A., Jr., Peters-Lidard, C. D., and Kumar, S. V.: Diagnosing the sensitivity of local land-atmosphere coupling via the soil moisture-boundary layer interaction, Journal of Hydrometeorology, 12, 766–786, https://doi.org/10.1175/jhm-d-10-05014.1, 2011.

Seifert, A., Bachmann, V., Filipitsch, F., Foerstner, J., Grams, C. M., Hoshyaripour, G. A., Quinting, J., Rohde, A., Vogel, H., Wagner, A., and Vogel, B.: Aerosol-cloud-radiation interaction during Saharan dust episodes: the dusty cirrus puzzle, Atmospheric Chemistry and Physics, 23, 6409–6430, https://doi.org/10.5194/acp-23-6409-2023, 2023.

Sharma, A., Sharma, D., Panda, S. K., and Kumar, A.: Sensitivity analysis of different parameterization schemes of the Weather Research and Forecasting (WRF) model to simulate heavy rainfall events over the Mahi River Basin, India, Agricultural and Forest Meteorology, 346, https://doi.org/10.1016/j.agrformet.2023.109885, 2024.

Shen, D., Li, N., Ran, L., Yin, L., Jiao, B., and Liu, Y.: Effects of a preexisting cold pool on the initiation of an extreme rainfall in southern Xinjiang, Atmospheric Research, 299, https://doi.org/10.1016/j.atmosres.2023.107151, 2024.

Thompson, G. and Eidhammer, T.: A study of aerosol impacts on clouds and precipitation development in a large winter cyclone, Journal of the Atmospheric Sciences, 71, 3636–3658, https://doi.org/10.1175/jas-d-13-0305.1, 2014.

Tian, J., Liu, R., Ding, L., Guo, L., and Liu, Q.: Evaluation of the WRF physical parameterisations for typhoon rainstorm simulation in southeast coast of China, Atmospheric Research, 247, https://doi.org/10.1016/j.atmosres.2020.105130, 2021.

Tian, L., Zhang, B., Wang, X., Chen, S., and Pan, B.: Large-scale afforestation over the Loess Plateau in China contributes to the local warming trend, Journal of Geophysical Research-Atmospheres, 127, https://doi.org/10.1029/2021jd035730, 2022.

van de Vyver, H., Van Schaeybroeck, B., De Troch, R., De Cruz, L., Hamdi, R., Villanueva-Birriel, C., Marbaix, P., van Ypersele, J. P., Wouters, H., Vanden Broucke, S., van Lipzig, N. P. M., Doutreloup, S., Wyard, C., Scholzen, C., Fettweis, X., Caluwaerts, S., and Termonia, P.: Evaluation framework for subdaily rainfall extremes simulated by regional climate models, Journal of Applied Meteorology and Climatology, 60, 1423–1442, https://doi.org/10.1175/jamc-d-21-0004.1, 2021.

Wang, Y., Sayit, H., Mamtimin, A., Zhu, J., Zhou, C., Huo, W., Yang, F., Yang, X., Gao, J., and Zhao, X.: Evaluation of five planetary boundary layer schemes in WRF over China's largest semi-fixed desert, Atmospheric Research, 256, https://doi.org/10.1016/j.atmosres.2021.105567, 2021.

Xu, Y., Zhang, L., and Hao, Z.: Drying and wetting trend in Xinjiang and related circulations background over the past 60 years, Environmental Research Communications, 6, https://doi.org/10.1088/2515-7620/ad7925, 2024.

Xu, Y., Zhang, L., Bai, M., Tian, S., and Hao, Z., 2026: Daily near-surface meteorological data for multiple WRF physics schemes over Xinjiang. Zenodo, https://doi.org/10.5281/zenodo.18182172.

Yang, J., Ji, Z., Chen, D., Kang, S., Fu, C., Duan, K., and Shen, M.: Improved land use and leaf area index enhances WRF-3DVAR satellite radiance assimilation: a case study focusing on rainfall simulation in the Shule River Basin during July 2013, Advances in Atmospheric Sciences, 35, 628–644, https://doi.org/10.1007/s00376-017-7120-4, 2018.

Yang, Q., Yu, Z., Wei, J., Yang, C., Gu, H., Xiao, M., Shang, S., Dong, N., Gao, L., Arnault, J., Laux, P., and Kunstmann, H.: Performance of the WRF model in simulating intense precipitation events over the Hanjiang River Basin, China – a multi-physics ensemble approach, Atmospheric Research, 248, https://doi.org/10.1016/j.atmosres.2020.105206, 2021.

Yang, T., Li, L., Hamdi, R., Cui, F., Zheng, Z., De Maeyer, P., and Chen, X.: Synergistic effects of precipitation and phase changes intensify future rain-on-snow events in the Tianshan and Pamir regions, Central Asia, Weather and Climate Extremes, 50, https://doi.org/10.1016/j.wace.2025.100833, 2025.

Yao, J., Chen, Y., Guan, X., Zhao, Y., Chen, J., and Mao, W.: Recent climate and hydrological changes in a mountain-basin system in Xinjiang, China, Earth-Science Reviews, 226, https://doi.org/10.1016/j.earscirev.2022.103957, 2022.

Yao, S., Jiang, D., and Zhang, Z.: Moisture sources of heavy precipitation in Xinjiang characterized by meteorological patterns, Journal of Hydrometeorology, 22, 2213–2225, https://doi.org/10.1175/jhm-d-20-0236.1, 2021.

Zhang, J., Wang, S., Huang, J., He, Y., and Ren, Y.: The precipitation-recycling process enhanced extreme precipitation in Xinjiang, China, Geophysical Research Letters, 50, https://doi.org/10.1029/2023gl104324, 2023a.

Zhang, M., Zhou, Y., Li, X., Sun, Z., Yang, G., and Xie, Z.: Quantifying the contributions of regional human activities and global climate change to the regional climate in a typical mountain-oasis-desert system of arid Central Asia from 1979 to 2018, Journal of Geophysical Research-Atmospheres, 128, https://doi.org/10.1029/2022jd037110, 2023b.

Zhang, S. Y., Wang, M. H., Wang, L. N., Liang, X. Z., Sun, C., and Li, Q. Q.: Sensitivity of the simulation of extreme precipitation events in China to different cumulus parameterization schemes and the underlying mechanisms, Atmospheric Research, 285, https://doi.org/10.1016/j.atmosres.2023.106636, 2023c.

Zhao, N., Manda, A., Guo, X., Kikuchi, K., Nasuno, T., Nakano, M., Zhang, Y., and Wang, B.: A Lagrangian view of moisture transport related to the heavy rainfall of July 2020 in Japan: importance of the moistening over the subtropical regions, Geophysical Research Letters, 48, https://doi.org/10.1029/2020gl091441, 2021.